

On the origin of soft X-rays in obscured AGN: answers from high-resolution spectroscopy with XMM-Newton

Matteo Guainazzi, Stefano Bianchi

European Space Astronomy Center of ESA, Apartado 50727, E-28080 Madrid, Spain

10 November 2018

ABSTRACT

We present results of a high-resolution soft X-ray (0.2–2 keV) spectroscopic study of a sample of 69 nearby obscured Active Galactic Nuclei (AGN) observed with the Reflection Grating Spectrometer (RGS) on board XMM-Newton. This is the largest sample ever studied with this technique so far. The main conclusions of our study can be summarized as follows: a) narrow Radiative Recombination Continua are detected in about 36% of the objects in our sample (in 26% their intrinsic width is ≤ 10 eV); b) higher order transitions are generally enhanced with respect to pure photoionization, indicating that resonant scattering plays an important role in the ionization/excitation balance. These results support the scenario, whereby the active nucleus is responsible for the X-ray “soft excess” almost ubiquitously observed in nearby obscured AGN via photoionization of circumnuclear gas. They confirm on a statistical basis the conclusions drawn from the detailed study of the brightest spectra in the sample. Furthermore, we propose a criterion to statistically discriminate between AGN-photoionized sources and starburst galaxies, based on intensity of the forbidden component of the OVII He- α triplet (once normalized to the OVIII Ly- α) coupled with the integrated luminosity in He-like and H-like oxygen lines.

Key words: galaxies:active – galaxies:nuclei – galaxies:Seyfert – X-rays:galaxies

1 INTRODUCTION

Nearby X-ray obscured Active Galactic Nuclei (AGN) invariably exhibit excess emission above the extrapolation of the absorbed nuclear emission (Turner et al. 1997; Guainazzi et al. 2005). The origin of this component - which can represent a significant fraction of the active nucleus bolometric energy budget (Levenson et al. 2002) - is still largely unknown. Gas in the nuclear environment could be heated to million degrees by shocks induced by AGN outflows (King 2005) or episodes of intense star formation (Cid Fernandes et al. 1998; Gonzalez-Delgado et al. 2001). Alternatively, the AGN primary emission could photoionize and photoexcite circumnuclear gas.

The latter scenario has recently received direct observational support, thanks to high-resolution capabilities in the spatial and frequency domains that large X-ray observatories such as *Chandra* and XMM-Newton nowadays offer. High-resolution spectra unveiled signatures of photoionized plasma in a few bright objects: NGC 1068 (Kinkhabwala et al. 2002; Young et al. 2001), the Circinus Galaxy (Sambruna et al. 2001), Mkn 3 (Sako et al. 2000; Bianchi et al. 2005; Pounds et al. 2005); NGC 4151 (Schurch et al. 2004). In

NGC 1068 the contribution of collisionally ionized plasma to the observed soft X-ray emission is constrained to be lower than 10% (Brinkman et al. 2002). These conclusions are based on three pieces of experimental evidence:

- (i) the spectra are dominated by strong emission lines of highly-ionized species from Carbon to Silicon, as well as by L-shell transitions from FeXVII to FeXXI
- (ii) narrow Radiative Recombination Continua (RRC) features from Carbon and Oxygen were detected. The width of these features indicates typical plasma temperatures of the order of a few eV (Kinkhabwala et al. 2002). These features are unequivocal signatures of photoionized spectra (Liedahl & Paerels 1996).
- (iii) the intensity of higher-order series emission lines, once normalized to the K α , are larger than predicted by pure photoionization, and are consistent with an important contribution by photoexcitation (resonant scattering) (Band et al. 1990; Matt 1994; Krolik et al. 1995). This explains why standard plasma diagnostics (Porquet & Dubau 2000) fail to properly interpret the physical nature of the spectra.

A solution in terms of AGN-photoionized gas can also

explain the coincidence in extension and overall morphology between soft X-ray emission and the Narrow Line Regions (NLRs), the latter traced by O[III] HST maps, on scales as large as a few hundred parsecs (Bianchi et al. 2006). Solutions satisfying the observed X-ray to optical flux ratio require an approximately constant ionization parameter (*i.e.*, a density scaling as the inverse square of the distance from the ionizing source), similarly to what is often found using photoionization models of the NLRs.

So far, high-resolution X-ray spectra have been published only for a few X-ray bright obscured AGN. However, diagnostically important emission lines in these objects exhibit very large Equivalent Widths, *EWs*, as the continuum is often totally suppressed in the soft X-ray band. In this *paper* we present the first systematic high-resolution X-ray spectroscopic study on a sizable sample of obscured AGN. The Reflection Grating Spectrometer (RGS) on board XMM-Newton (der Herder et al. 2001) is the most suitable instrument currently flying for this purpose, due to its unprecedented effective area in the 0.2-2 keV band, as well as its good absolute aspect solution accuracy ($\simeq 8$ mÅ).

2 CIELO-AGN

2.1 The sample

Our sample comprises all the type ≥ 1.5 AGN (according to the NED classification) observed by XMM-Newton, and whose data were public as of September 2006 (Tab. 1 shows the list of sources in the sample, together with their redshift and the combined exposure time for one RGS camera). After excluding H1320+551 and H1419+480 due to uncertainties in their classification, the sample includes 69 sources.

2.2 Data processing

For each observation, we have reprocessed RGS data starting with the *Observation Data Files*, using SASv6.5 (Gabriel et al. 2003), and the most advanced calibration files available as of May 2006. Background spectra were generated using blank field event lists, accumulated from different positions on the sky vault along the mission. Spectra of the same source from different observations were merged, together with their response matrices, after checking that no significant spectral variability occurred.

Each spectrum was systematically searched for the presence of emission lines. We simultaneously fit together the spectra of the two RGS cameras, using XSPEC version 12.3.0. “Local” fits to the data were performed on the unbinned spectra on $\simeq 100$ channels wide intervals, using Gaussian profiles to account for any line features. In only a few cases (see Tab. 2) the width of the profiles accounting for bound-bound transitions is inconsistent with zero; hence in these cases only the intrinsic profile width has been left free in the fit. On the other hand, free-bound transitions were modeled with Gaussian profiles, where the intrinsic width was always considered an additional free fit parameter. We have always assumed the same intrinsic width for the components of a multiplet. Local continua were modeled with $\Gamma = 1$ power-laws, leaving free in each fit the continuum normalization (Γ is the power-law photon index). No assumption was made *a*

Table 1. CIELO-AGN sources.

Source	z	Exposure time (ks)
Circinus Galaxy	0.001	102.2
ESO509-G66	0.045	13.6
IC2560	0.010	81.4
IC4395	0.036	22.1
IC4995	0.016	11.5
IIZW035	0.027	20.7
IRAS01475-0740	0.018	11.5
IRAS08572+3915	0.058	28.6
IRAS09104+4109	0.442	13.5
IRAS10214+4724	2.286	53.4
IRAS13197-1627	0.017	44.6
IRAS15480-0344	0.030	10.9
MCG-5-23-16	0.009	61.6
MRK3	0.014	180.8
MRK6	0.019	96.4
MRK331	0.019	17.9
MRK348	0.015	46.3
MRK612	0.020	11.8
MRK744	0.009	22.7
MRK993	0.015	22.6
MRK1152	0.053	26.4
NGC1068	0.004	86.8
NGC1365	0.005	127.5
NGC1386	0.003	16.9
NGC1410	0.025	11.7
NGC1614	0.016	23.5
NGC2110	0.008	51.7
NGC2273	0.006	12.5
NGC2623	0.019	12.3
NGC2992	0.008	28.5
NGC34	0.020	21.8
NGC3982	0.004	34.0
NGC4138	0.003	14.3
NGC4151	0.003	55.5
NGC4168	0.007	23.0
NGC424	0.012	7.9
NGC4258	0.002	78.5
NGC4303	0.005	42.8
NGC4395	0.001	108.4
NGC4472	0.003	1.5
NGC4477	0.004	13.3
NGC449	0.016	11.9
NGC4507	0.012	44.5
NGC4565	0.004	14.4
NGC4639	0.003	14.6
NGC4725	0.004	17.6
NGC4945	0.002	63.8
NGC4968	0.010	11.8
NGC5033	0.003	19.7
NGC5252	0.023	65.8
NGC526A	0.019	46.9
NGC5273	0.004	16.1
NGC5506	0.006	32.9
NGC5643	0.004	9.6
NGC591	0.015	11.8
NGC6552	0.026	6.8
NGC7172	0.009	72.0
NGC7212	0.027	13.7
NGC7314	0.005	43.4
NGC7479	0.008	12.6
NGC7582	0.005	22.3
NGC7674	0.029	10.3
UGC1214	0.017	11.8
UGC2456	0.012	17.1
UGC2608	0.023	7.5
UGC4203	0.014	7.8
UGC6527	0.027	23.6
UGC8621	0.020	11.8
UM625	0.025	11.6

priori on the line centroid energies.¹ However, fits of He- α triplets have been performed keeping the relative distance between the centroid energies of the components fixed to the value dictated by atomic physics. A line is considered to be detected when its flux is inconsistent with 0 at the $1\text{-}\sigma$ level. In Appendix A we list energies, fluxes and intrinsic widths (for the RRC only) of the transitions individually presented in this paper, and discuss the consistency of our measurements with the expected laboratory energies [laboratory energies are extracted from the CHIANTI database (Dere et al. 2001)]. Line luminosities have been corrected for Galactic photoelectric absorption using column densities after Dickey & Lockman (1990).

We have as well checked whether the detected line energy centroids in each source were systematically shifted

¹ On the other hand, upper limits on the line intensities were calculated assuming the laboratory energies.

Table 2. $1\text{-}\sigma$ intrinsic widths for resolved Gaussian profiles in *CIELO-AGN*.

Transition	Width (km s^{-1})
NGC1068	
Fexvii 3d-2p (1P_1)	$670 \pm_{10}^{110}$
Nvii Ly- α	$820 \pm_{40}^{80}$
Ovii He- α	$550 \pm_{20}^{50}$
Ovii He- β	$3300 \pm_{600}^{200}$
Ovii He- γ	$650 \pm_{50}^{150}$
Oviii Ly- α	$460 \pm_{40}^{60}$
Oviii Ly- β	$1000 \pm_{20}^{200}$
NGC4151	
Fexviii 3s-2p	$1100 \pm_{600}^{900}$
Cvi Ly- α	$490 \pm_{80}^{150}$
Cvi Ly- β	$900 \pm_{400}^{700}$
NGC4507	
Ovii He- α	$520 \pm_{190}^{110}$

with respect to the laboratory energies. We define “systematic” energy shifts different from zero (in the same direction) at the 1σ level in at least two of the following transitions: Cvi Ly- α , Ovii He- α , Ovii He- β , and Oviii Ly- α . Our analysis found none of these systematic shifts. Nonetheless, we found some occurrences of discrepancies between the best-fit centroid and the laboratory energies in individual lines. We refrain from attributing any astrophysical meaning to these discrepancies, which may be due to contamination by nearby transitions, residual errors in the aspect solution of the RGS cameras, or spurious detections. The reader may find a more detailed discussion of this point in the Appendix.

In Fig. 1 we show the RGS spectra of the three still unpublished Seyfert 2 galaxies in our sample, which exhibit the largest number of line detections.

Hereafter, uncertainties on the fitting parameters are quoted at the 1σ level; likewise the upper limits represent a 1σ confidence level. Errors on the line centroid energies include a 8 mÅ systematic error. Throughout this paper, energies/wavelengths of astrophysical lines are quoted in the source rest frame, unless otherwise specified.

2.3 The catalog

The results of the procedure outlined above have been compiled into **CIELO-AGN** (*Catalog of Ionized Emission Lines in Obscured AGN*). Our study exhibit a high-detection efficiency, at least with respect to the most common lines observed in obscured AGN spectra, despite the overall low soft X-ray flux (sample median 6×10^{-13} erg cm^{-2} s^{-1} ; see Tab. 3 for a complete list of the lines detected in *CIELO-AGN*).

3 RESULTS

In this Section we will use some results of our study to try and answer the following questions on the nature of soft X-ray emission in obscured AGN:

- is AGN photoionization the dominant physical process?

Table 3. Number of *CIELO-AGN* sources, N_{det} , for which a given *Transition* (laboratory wavelength λ_{lab}) has been detected, if $N_{det} > 0$

Transition	λ_{lab} (Å)	N_{det}
Sixiii He- α	6.740	5
Mgxii He- α (<i>r</i>)	9.228	12
Mgxii He- α (<i>f</i>)	9.314	13
Nex Ly- α	12.134 ^a	20
Fexxi 3d-2p	12.282	21
Fexx 3d-2p	12.845	19
Neix He- α (<i>r</i>)	13.447	13
Neix He- α (<i>i</i>)	13.553	6
Neix He- α (<i>f</i>)	13.699	15
Oviii RRC	14.228	13
Fexviii 3d-2p	14.413 ^b	24
Oviii Ly- δ	14.821 ^c	20
Fexvii 3d-2p (1P_1)	15.015	25
Fexvii 3d-2p (3D_1)	15.262	24
Oviii Ly- β	16.006	22
Fexviii 3s-2p	16.091	23
Ovii RRC	16.771	17
Fexvii 3s-2p (3G/M2)	17.076 ^d	27
Ovii He- γ	17.768 ^e	16
Ovii He- β	18.627	20
Oviii Ly- α	18.967	30
Ovii He- α (<i>r</i>)	21.602	22
Ovii He- α (<i>i</i>)	21.803	13
Ovii He- α (<i>f</i>)	22.101	23
Nevii Ly- α	24.782 ^f	24
Cvi Ly- β	28.459 ^g	14
Nvi He- α	28.787	11
Cv RRC	31.622	6
Cvi Ly- α	33.737 ^h	23

^adoublet: $\lambda_1 = 12.1321$ Å, $\lambda_2 = 12.1375$ Å

^btriplet: $\lambda_1 = 14.3760$ Å, $\lambda_2 = 14.4187$ Å, $\lambda_3 = 14.4210$ Å

^cpossible contamination by Fexx $3p^2\text{-}2p^2$ at $\lambda = 14.8501$ Å

^ddoublet: $\lambda_1 = 17.0500$ Å, $\lambda_2 = 17.0970$ Å

^epossible contamination by Fexviii $3p^2\text{-}2p^2$ at $\lambda = 17.8472$ Å

^fdoublet: $\lambda_1 = 24.7790$ Å, $\lambda_2 = 24.7840$ Å

^gdoublet: $\lambda_1 = 28.4612$ Å, $\lambda_2 = 28.4662$ Å

^hdoublet: $\lambda_1 = 33.7342$ Å, $\lambda_2 = 33.7396$ Å

- does resonant scattering play an important role?
- do efficient X-ray line diagnostics exist, which could allow us to discriminate on a statistical basis between AGN- and starburst-powered spectra?

3.1 RRC

The three most intense RRC transitions in the RGS energy bandpass are: Oviii at 14.228Å, Ovii at 16.771Å and Cv at 31.622Å. At least one of these features is detected in 36% (25/69) of the objects of our sample. The few measurements of the RRC width, which represents a direct estimate of the temperature of the plasma (Liedahl & Paerels 1996), cluster in the range 1–10 eV. There is an obvious selection effect, favoring the detection of narrow features. Nonetheless, still in 29% (26%) of the objects in our sample the RRC width is constrained to be lower than 50 (10) eV (see Fig. 2). In 10 further objects we detect upper limits on the RRC luminosity in the range where measurements are found: in 7 (10)

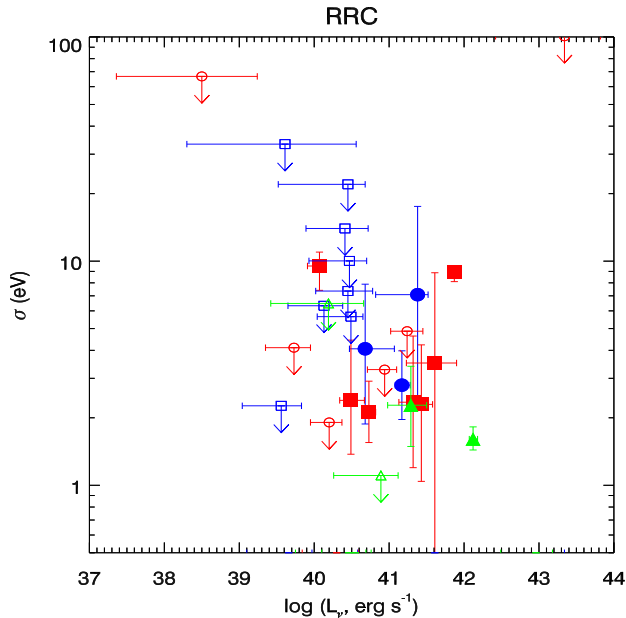


Figure 2. Luminosity versus intrinsic width for the RRC features detected in our sample. *Filled* data points correspond to a measurement of the RRC width; *empty* data points correspond to RRC width upper limits. *Circles*: OVIII; *squares*: OVII; *triangles*: Cv. Data points corresponding to upper limits on both quantities are not shown for clarity.

of them the luminosity is constrained to be $\leq 10^{41.1}$ erg s $^{-1}$ ($\leq 10^{44.2}$ erg s $^{-1}$). Finally, in 34/69 (49%) of the objects the quality of the data is too poor to allow a significant detection of any of the RRC features, and the upper limits on their luminosities are inconclusive.

In principle, measurements of the OVII RRC could be contaminated by the 3F component of the FeXVII triplet at 16.780Å (Brown et al. 1998). However, the intensity ratio between the OVII RRC and the 3G/M2 components of the same triplet (which cannot be resolved by the RGS) exceeds 0.6, the largest expected value if the former feature were entirely due to the 3F component (Phillips et al. 1997; Mauche et al. 2001; Beiersdorfer et al. 2002), in 15 out of 16 cases (by more than a factor of 2 in 13 out of 16; cf Fig. 3). We are therefore confident that most of our measurements of the the emission line at 16.777Å represent *bona fide* detections of the OVII RRC. The total number of sources for which at least one RRC feature is detected is reduced by 1 if the effect of this potential mis-identification is taken into account.

3.2 Higher order series

In addition to $n = 2p \rightarrow 1s$ transitions for H- and He-like atoms, *CIELO-AGN* contains a fair number of detections of discrete higher order resonance transitions ($np \rightarrow 1s$, $n > 2$). These transitions are selectively enhanced by photoexcitation. Since the forbidden f transition in He-like triplets is unaffected by photoexcitation, the intensity ratio between higher order series and f transition intensities provides a potentially powerful diagnostic of the importance of resonant scattering in radiation ionized spectra (Kinkhabwala et al. 2002). An example of the application of this diagnos-

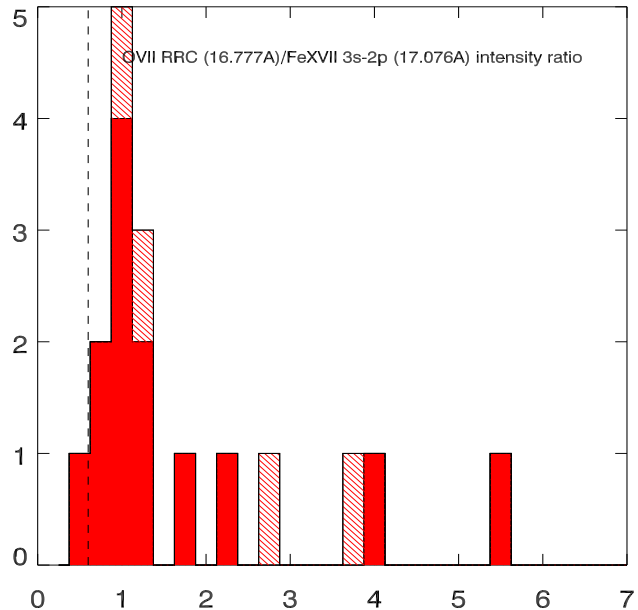


Figure 3. Observed intensity ratio between the 16.777Å and the 17.076Å features in *CIELO-AGN*. *Shaded cells* indicate lower limits. The *dashed line* represents the maximum expected ratio, if both features are due to the FeXVII triplet. In 15 out of 16 cases, the observed ratio exceeds this limit, indicating that OVII must be the dominant transition at 16.777Å.

tic test to *CIELO-AGN* is shown in Fig. 4, where we display the intensity of the OVII He- β against the f component of the OVII He- α triplet. We compare the experimental results with the predictions of pure photoionization, and with models where radiative decay from photoionization and recombination from photoionization are self-consistently calculated (model `photoion`; Kinkhabwala et al. 2002). We have produced a grid of models for different values of OVII column densities ($N_{OVII} \in [10^{15}, 10^{20}$ cm $^{-2}$]), turbulence velocities ($v_{turb} \in [0, 500$ km s $^{-1}$]), and temperatures ($kT \in [1, 20$ keV]). The weighted mean of the He- β versus f intensity ratio is 0.25 ± 0.03 , larger than expected for pure photoionization. It corresponds to OVII column densities $N_{OVII} \simeq 10^{17-18}$ cm $^{-2}$ (the dependence on the other parameters is small). The measurements on the He- β OVII transition at 18.6270Å could be contaminated by the nearby NVII RRC at 18.5872Å 2 . In order to minimize this contamination, we fit the X-ray spectra around the OVII He- β feature in a range, which in principle does not include the contaminating feature. Moreover, we have verified that similar enhancements of higher-order lines to the Lyman- α of H-like Carbon and Oxygen are observed as well (cf. Tab. 4). The dependence on the temperature, column density and velocity distributions in H-like species is such that no meaningful constraints on column density can be drawn. However, in 8 of the individual brightest sources in our sample 3 the ratio between the OVIII Ly- β and Ly- α

2 For instance, the OVII He- β width measured in in NGC 1068, $\sigma = 73 \pm_{13}^5$ eV (cf. Tab. 2), the largest measured in this spectrum, is most likely contaminated by the NVII RRC

3 the Circinus Galaxy, IRAS 13197-1627, Mrk 3, NGC1068, NGC1365, NGC2110, NGC2992, NGC4945

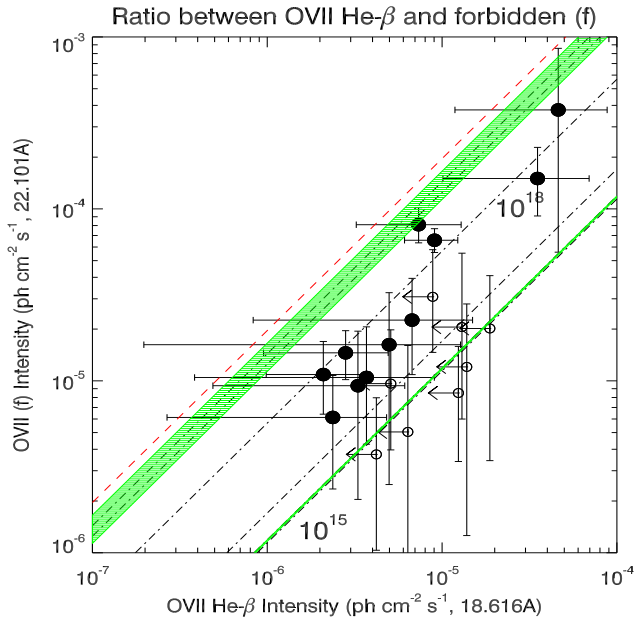


Figure 4. Intensity of OVII He- β line against the intensity of the f component of the He- α triplet (only data points corresponding to a detection of the latter are shown; data points correspond to upper limits on the intensity of the former are shown as empty symbols). The dashed-dotted lines represent the prediction of the photoion code for OVII column densities increasing from $N_{OVII} = 10^{15}$ to 10^{20} cm^{-2} in steps of one decade, assuming $kT = 5$ eV and $v_{turb} = 200$ km s^{-1} . The long-dashed line represents the predictions for pure photoionization. The shaded areas represent the loci of the photoion predictions, when the turbulent velocity varies in the range 0–500 km s^{-1} at constant temperature and for the extreme values of the column density interval. The areas representing a variation of the temperature in the range 1–20 keV at constant velocity and column density are comparatively smaller, and therefore not shown.

Table 4. Higher-order intensity ratios for selected transitions in *CIELO-AGN*. Each ratio is calculated as the weighted mean of the individual ratios on the N sources, where a measurement of both transitions is available, and using the statistical uncertainties on the ratio as weights. Expected values for pure photoionization (PIE) and collisional ionization (CIE) are extracted from Tab. 3 in Kinkhabwala et al. (2002)

Ion	Ratio	N	PIE	CIE
CvI Ly- β /Ly- α	0.51 ± 0.12	9	0.14	0.09
OVII He- β / f	0.25 ± 0.03	12	0.05	...
OVII He- γ / f	0.20 ± 0.09^a	9	0.017	...
O VIII Ly- β /Ly- α	0.35 ± 0.05	13	0.14	0.10

^athis measurement is likely to be affected by contamination of FeXVIII 3p²-2p² at $\lambda = 17.8472$ Å

intensities is large enough to be formally inconsistent with collisional ionization, and in 4 of them⁴ with pure photoionization as well.

⁴ NGC1068, NGC1365, NGC2110, NGC2992

Source	z	Exposure time (ks)
ARP244	0.006	75.0
ARP270	0.005	36.6
HolmbergII	0.000	30.6
IZw18	0.003	52.3
M82	0.001	141.6
M83	0.002	30.5
MCG-5-31-7	0.010	19.0
NGC1313	0.002	241.4
NGC1482	0.006	17.9
NGC1511	0.004	44.0
NGC1705	0.002	58.5
NGC2146	0.003	35.9
NGC2403	0.000	43.5
NGC253	0.001	192.3
NGC2798	0.006	13.8
NGC3256	0.009	16.7
NGC3310	0.003	19.2
NGC3690	0.010	21.5
NGC4214	0.001	19.5
NGC4449	0.004	28.1
NGC474	0.008	25.4
NGC5073	0.009	51.8
NGC520	0.008	12.6
NGC5253	0.001	45.8
NGC660	0.003	11.9
NGC7552	0.005	24.0
NGC7714	0.009	41.3

Table 5. Log of the XMM-Newton observations of the starburst galaxies in the control sample

3.3 AGN and starburst soft X-ray spectra

We have analyzed the RGS spectra of a sample of 27 Starburst (SB) galaxies extracted from the Wu et al. (2002) sample (cf. Tab. 5) and observed by XMM-Newton, to identify diagnostic criteria, which may allow us to statistically discriminate between SB- and AGN-dominated soft X-ray spectra. This sample has been analyzed in the same way as the Seyfert 2 sample. Some of the criteria quoted in the literature provide inconclusive results. For instance, the distribution functions of the luminosity ratio between L shell iron and integrated oxygen He- and H-like lines are indistinguishable (Fig. 5). Kallman et al. (1996) had already pointed out that L-shell iron transitions can give an important contribution to the overall luminosity budget in photoionized nebulae. The standard G ratio ($G \equiv (f + i)/r$; Gabriel & Jordan 1969; Porquet et al. 2000), is also ambiguous. Previous studies have shown (c.f. Sect. 1) that the enhancement of resonant lines by resonant scattering mimics the behavior of a collisionally ionized plasma. In the collisionally ionized case, the fluxes of all the triplet lines are enhanced, with the greatest increase in the resonance line. Resonant scattering boosts all of the resonant lines with respect to the forbidden and intercombination lines in the triplet. The value of G is therefore decreased by both collisional excitation and resonant scattering. Finally, the fraction of SB spectra where narrow RRC features are detected is comparable to that observed in the Seyfert 2 sample, indicating that photoionization plays an important role in the ionization balance of starburst galaxies as well.

In Fig. 6 we compare the distribution of the OVII f transition intensity, normalized against the intensity of the OVIII Ly- α , as a function of the total luminosity in oxygen lines (integrated on all He- and H-like transitions). AGN are generally characterized by larger intensity ratios, η : $\eta_{AGN} = 1.38 \pm_{0.12}^{0.13}$, $\eta_{SB} = 0.57 \pm_{0.09}^{0.07}$ (5.8 σ difference; the upper limits have been taken into account with a “bootstrap” method for censored data as in Schmitt 1985). The same figure also shows that the average line luminosity in AGN is larger than in starbursts. The median Oxygen lines

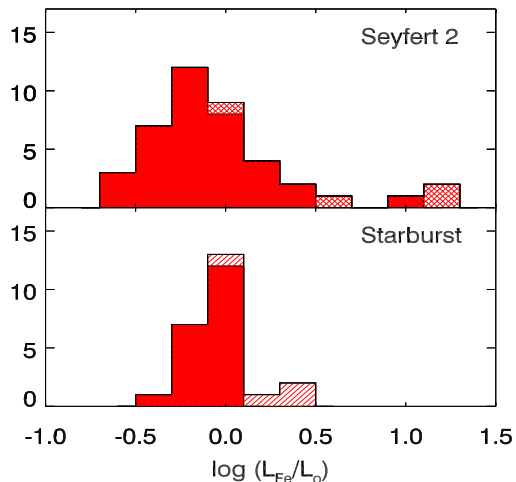


Figure 5. Distribution function for the logarithm of the ratio of the integrated luminosities in the iron and oxygen lines for our Seyfert 2 (*lower panel*) and in the control sample of starburst galaxies (*lower panel*). *Diagonally shaded cells* indicate upper limits, *checked cells* indicate lower limits. The medians of the two distributions are very similar: -0.10 and -0.08 , respectively.

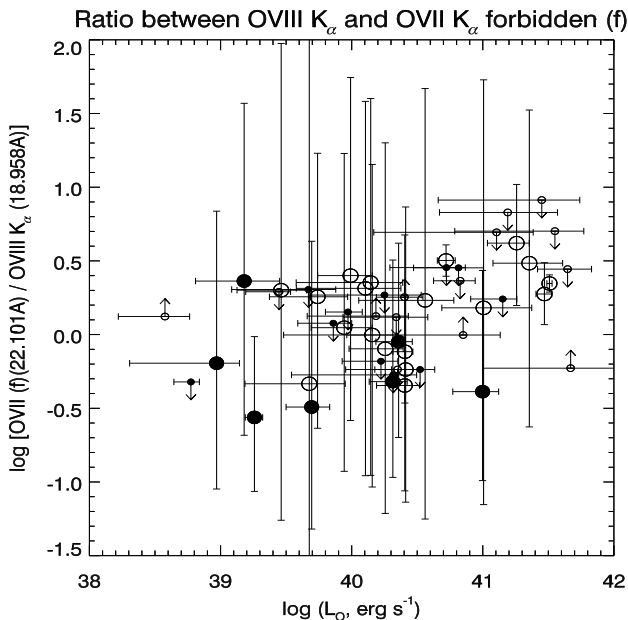


Figure 6. Intensity of the f component of the OVII triplet (normalized to the OVIII Ly- α intensity) against the total luminosity in Oxygen lines. *Empty circles* represents the obscured AGN in *CIELO-AGN*, *filled circles* the control sample of 27 starburst galaxies. Symbols representing censored data are plotted with a smaller size for the sake of clarity.

luminosity is $\sim 10^{41}$ erg s $^{-1}$ in the former and $\sim 10^{40}$ erg s $^{-1}$ in the latter (using strict detections only). Still, the overlap between the line diagnostic distributions is significant, and prevents strong statements on individual sources. This most likely reflects the intrinsic “composite” nature of several obscured AGN (Cid Fernandes et al. 2001).

4 CONCLUSIONS

In this paper we present results from a systematic study of high-resolution soft X-ray spectra for 69 obscured AGN observed with the XMM-Newton RGS. Our main conclusions can be summarized as follows:

- **Radiative Recombination Continua:** we detect RRC features in about 40% of the sample sources, and in 33% (27%) they allow us to constraint the temperature of the plasma ≤ 50 eV (≤ 10) eV. This indicates that in a large fraction of objects in our sample photoionization dominates the ionization balance. Still, these percentages represent probably lower limits to the true fraction of photoionized sources in our sample: upper limits on narrow RRC features in almost 50% of the objects in our sample are still inconclusive due to the lack of statistics

- **Resonant scattering:** higher order transitions are enhanced with respect to the expectation of pure photoionization, and inconsistent with the expectation of collisional ionization as well. This indicates that resonant scattering plays an important role in the ionization/excitation balance. The observed OVII He- β versus f intensity ratios are consistent with OVII column densities in the range $N_{OVII} \sim 10^{17-18}$ cm $^{-2}$. Interestingly enough, these values are in good agreement with the column densities measured in “warm absorbers” observed along the lines of sight to unobscured AGN (Blustin et al. 2003; Steenbrugge et al. 2005; Blustin et al. 2005).

- **Starburst contribution:** the comparison between the spectra of obscured AGN in our sample and a control sample of nearby starburst galaxies suggests two empirical criteria to discriminate *on a statistical basis* between AGN- and starburst-powered spectra: a) total Oxygen line X-ray luminosity $\gtrsim 10^{40}$ erg s $^{-1}$; b) ratio between the OVII triplet f component and the OVIII Ly- α $\gtrsim 1$.

The currently available X-ray instrumentation allowed us to explore the nature of the soft X-ray emission in obscured AGN as weak as ~ 0.03 mCrab. From this study, we have gained confidence that conclusions on the properties of the gas in the circumnuclear region of AGN extracted from the detailed study of high-quality spectra of the brightest objects can be extended to the whole population of nearby obscured AGN. This is the main message we would like to convey with this *paper*, which opens interesting perspectives for future enlargements of this study once deeper exposures or more sensitive instrumentation are available.

APPENDIX

The tables in this Section list centroid energies and fluxes for the bound-bound transitions individually discussed in this paper: CVI Ly- α , CVI Ly- β , OVII He- α , OVII He- β , OVIII Ly- α , and OVIII Ly- β (Tab. 6 to 7). The same quantities are listed for the Cv, OVII, and OVIII RRCs, alongside their intrinsic width (Tab. 8 to 9).

The comparison between the best-fit centroid energy of detected lines in *CIELO-AGN* and the laboratory energies is an instructive exercise on the reliability of the catalog measurements. At the 2σ level, the number of He- and H-like Oxygen lines (out the total detected ones) which are inconsistent with the laboratory energies are: 0/25, 2/20, 2/30 and

Source	Cvi Ly- α (Å, 33.737)	Cvi Ly- β (Å, 28.459)	Ovii He- α (r) (Å, 21.602)	Ovii He- β (Å, 18.627)	Oviii Ly- α (Å, 18.967)	Oviii Ly- β (Å, 16.006)
Circinus Galaxy	21.689 \pm 0.754	18.616 \pm 0.052	18.941 \pm 0.040	15.999 \pm 0.048
ESO509-G66
IC2560	21.598 \pm 0.543	18.640 \pm 0.054	...	16.075 \pm 0.087
IC4395
IC4995	33.430 \pm 0.086
IIZW035
IRAS01475-0740
IRAS08572+3915
IRAS09104+4109
IRAS10214+4724
IRAS13197-1627	18.700 \pm 0.177	18.931 \pm 0.050	16.015 \pm 0.049
IRAS15480-0344
MCG-5-23-16	21.597 \pm 0.557	18.664 \pm 0.074
MRK3	18.615 \pm 0.038	...	16.022 \pm 0.061
MRK6
MRK331	18.367 \pm 0.392
MRK348	33.415 \pm 0.074	19.013 \pm 0.115	...
MRK612
MRK744
MRK993
MRK1152
NGC1068	21.576 \pm 0.029	18.685 \pm 0.044	18.962 \pm 0.029	16.006 \pm 0.033
NGC1365	33.767 \pm 0.052	28.491 \pm 0.053	21.600 \pm 0.028	18.634 \pm 0.032	18.966 \pm 0.030	16.030 \pm 0.047
NGC1386	33.776 \pm 0.050	...	21.592 \pm 0.029	...	18.933 \pm 0.030	...
NGC1410
NGC1614	18.598 \pm 0.183
NGC2110	33.397 \pm 0.065	18.663 \pm 0.071	18.994 \pm 0.047	16.181 \pm 0.051
NGC2273
NGC2623
NGC2992	...	28.076 \pm 0.059	21.598 \pm 0.051	...	18.941 \pm 0.053	15.802 \pm 0.054
NGC34
NGC3982	18.813 \pm 0.052	...
NGC4138	33.988 \pm 0.063	28.400 \pm 0.298	21.563 \pm 0.658	...	19.245 \pm 0.072	...
NGC4151	33.740 \pm 0.083	28.439 \pm 0.107
NGC4168	18.361 \pm 0.053	...	15.779 \pm 0.062
NGC424	33.733 \pm 0.118	...	21.612 \pm 0.552	...	18.923 \pm 0.065	...
NGC4258	33.617 \pm 0.097	28.506 \pm 0.047	19.044 \pm 0.061	15.961 \pm 0.187
NGC4303	21.636 \pm 0.050	...	18.971 \pm 0.081	15.961 \pm 0.100
NGC4395	33.895 \pm 0.066	...	21.589 \pm 0.535	18.740 \pm 0.092	...	15.819 \pm 0.052
NGC4472	16.078 \pm 0.050
NGC4477	33.747 \pm 0.068	28.152 \pm 0.086	18.992 \pm 0.072	16.078 \pm 0.047
NGC449	21.602 \pm 0.561
NGC4507	34.025 \pm 0.830	...	21.601 \pm 0.828	18.651 \pm 0.062	18.958 \pm 0.044	16.018 \pm 0.109
NGC4565	18.719 \pm 0.046	...	15.857 \pm 0.179
NGC4639	...	28.549 \pm 0.084
NGC4725	33.731 \pm 0.231	28.236 \pm 0.085	21.589 \pm 0.554	...	18.974 \pm 0.038	...
NGC4945	18.986 \pm 0.053	...
NGC4968	18.986 \pm 0.080	16.104 \pm 0.074
NGC5033	...	28.657 \pm 0.053	21.586 \pm 0.537	16.074 \pm 0.032
NGC5252	33.370 \pm 0.112	19.025 \pm 0.048	16.178 \pm 0.045
NGC526A	18.896 \pm 0.153	16.178 \pm 0.108
NGC5273	...	28.668 \pm 0.092	21.609 \pm 0.530	18.556 \pm 0.129
NGC5506	33.819 \pm 0.039	28.375 \pm 0.068	21.573 \pm 0.516	18.632 \pm 0.069
NGC5643	34.018 \pm 0.123	...	21.573 \pm 0.059	18.632 \pm 0.121	...	16.001 \pm 0.110
NGC591	18.976 \pm 0.053	...
NGC6552	18.974 \pm 0.125	...
NGC7172	21.566 \pm 0.042	...	18.977 \pm 0.052	...
NGC7212
NGC7314	21.602 \pm 0.047	...	18.977 \pm 0.076	...
NGC7479	18.868 \pm 0.080	...
NGC7582	33.676 \pm 0.059	...	21.603 \pm 0.049	18.624 \pm 0.123	18.948 \pm 0.093	...
NGC7674	18.960 \pm 0.043	...
UGC1214	33.545 \pm 0.057	28.349 \pm 0.102	18.956 \pm 0.034	16.065 \pm 0.141
UGC2456	33.595 \pm 0.069	18.634 \pm 0.073	18.956 \pm 0.053	16.065 \pm 0.139
UGC2608	15.836 \pm 0.044
UGC4203	33.797 \pm 0.122
UGC6527	16.022 \pm 0.103
UGC8621
UM625

Table 6. Best-fit wavelengths for the transitions discussed in this *paper*. *Dots* indicates either lines not detected, or lines for which no constraints can be obtained (the luminosities in Tab. 7 are calculated in this case assuming the laboratory energies). In the table header, the laboratory wavelengths are in brackets.

5/22 for OVII He- α , OVII He- β , OVIII Ly- α and OVIII Ly- β , respectively. The shifted measurements in the last case cluster around 783 eV (4 out of 5), where a strong FeXVIII 3s2p transition is located ($\lambda = 15.83$ Å), and are therefore probably due to a mis-identification. If we remove these suspicious cases, the ratio between the He- β and the f transition intensity in the remaining objects is still inconsistent with the

expectation of pure photoionization: 0.26 ± 0.04 (cf. Tab. 4). The situation for the Cvi lines is more controversial. The centroid energies of 6 out of 23 Ly- α and 5 out of 14 Ly- β measurements are inconsistent at the 2σ level with the laboratory energies. There is no obvious explanation for these systematic discrepancies. No other potentially contaminating transition is present, which could confuse the identifi-

Source	CVI Ly- α 10^{-5} ph cm $^{-2}$ s $^{-1}$	CVI Ly- β 10^{-5} ph cm $^{-2}$ s $^{-1}$	OVII He- α 10^{-5} ph cm $^{-2}$ s $^{-1}$	OVII He- β 10^{-5} ph cm $^{-2}$ s $^{-1}$	OVIII Ly- α 10^{-5} ph cm $^{-2}$ s $^{-1}$	OVIII Ly- β 10^{-5} ph cm $^{-2}$ s $^{-1}$
Circinus Galaxy	37.6 \pm 48.2 32.0	4.6 \pm 4.1 3.4	14.9 \pm 7.3 6.0	3.6 \pm 1.9 1.6
ESO509-G66
IC2560	1.0 \pm 0.6 0.4	0.2 \pm 0.1	...	0.1 \pm 0.1 0.0
IC4395
IC4995	1.6 \pm 2.4 1.4
IIZW035
IRAS01475-0740
IRAS08572+3915
IRAS09104+4109
IRAS10214+4724
IRAS13197-1627	15.0 \pm 7.7 5.9	3.5 \pm 3.4 2.5	1.0 \pm 0.5 0.4	0.4 \pm 0.3 0.2
IRAS15480-0344
MCG-5-23-16	1.6 \pm 1.6 1.3	0.4 \pm 0.4 0.1
MRK3	6.5 \pm 1.0 0.9	0.9 \pm 0.3 0.2	3.4 \pm 0.4 0.4	0.7 \pm 0.2 0.2
MRK6
MRK331	0.4 \pm 0.6 0.3
MRK348	2.5 \pm 2.3 1.8	1.2 \pm 1.1 1.0	...
MRK612
MRK744
MRK993
MRK1152
NGC1068	98.6 \pm 4.6 4.5	10.9 \pm 1.5	124.9 \pm 4.6 3.6	44.3 \pm 3.3 3.1	53.2 \pm 2.1 2.1	14.9 \pm 1.2 1.1
NGC1365	1.1 \pm 0.5 0.4	0.4 \pm 0.2 0.1	1.4 \pm 0.3 0.4	0.2 \pm 0.2 0.1	1.9 \pm 0.3 0.3	0.5 \pm 0.2 0.1
NGC1386	0.9 \pm 0.4 0.7	...	1.8 \pm 0.4 0.9	...	1.0 \pm 0.7 0.5	...
NGC1410
NGC1614	0.4 \pm 0.5 0.4
NGC2110	9.6 \pm 10.1 7.1	0.6 \pm 0.7 0.5	1.2 \pm 0.8 0.6	1.5 \pm 0.8 0.6
NGC2273
NGC2623
NGC2992	...	1.0 \pm 0.8 0.7	1.2 \pm 1.5 1.0	...	0.7 \pm 0.7 0.6	1.2 \pm 1.0 0.8
NGC34
NGC3982	1.4 \pm 1.3	...	0.7 \pm 0.7 0.5	...
NGC4138	0.9 \pm 1.2 0.6	0.4 \pm 0.7 0.4	0.5 \pm 1.1 0.4	...	1.0 \pm 0.7 0.3	...
NGC4151	17.7 \pm 2.0	2.0 \pm 0.8 0.7	49.5 \pm 3.1	1.3 \pm 0.8 0.7	15.5 \pm 1.3 1.2	2.5 \pm 0.6 0.5
NGC4168	0.2 \pm 0.3 0.2	...	0.2 \pm 0.4 0.2
NGC424	2.0 \pm 2.3 1.4	...	3.0 \pm 2.7 1.6	...	1.0 \pm 0.9 0.4	...
NGC4258	0.6 \pm 0.6 0.5	0.5 \pm 0.4 0.3	...	1.9 \pm 0.6 0.5	0.6 \pm 0.4 0.4	0.3 \pm 0.3 0.3
NGC4303	41.6 \pm 29.9 2.8	...	0.5 \pm 0.7	...	0.7 \pm 0.4	...
NGC4395	0.6 \pm 0.3 0.3	...	0.6 \pm 0.3 0.3	0.2 \pm 0.2 0.2	...	0.3 \pm 0.2 0.2
NGC4472	7.9 \pm 4.9 4.9
NGC4477	1.6 \pm 1.9 1.2	0.9 \pm 1.2 0.8	0.8 \pm 0.9 0.6	...
NGC449	2.0 \pm 3.4 1.4
NGC4507	67.6 \pm 65.2 65.2	...	8.0 \pm 2.0 1.7	0.7 \pm 0.5 0.5	1.9 \pm 0.7 0.5	0.2 \pm 0.3 0.4
NGC4565	0.2 \pm 0.3 0.1	...	0.3 \pm 0.4 0.2
NGC4639	...	0.7 \pm 1.0 0.6
NGC4725	0.7 \pm 1.1 0.7	0.5 \pm 0.7 0.4	0.9 \pm 1.0	...	0.8 \pm 0.6	...
NGC4945	9.3 \pm 12.5 8.0	...	1.9 \pm 2.8 1.5	...	0.9 \pm 1.3 0.8	0.4 \pm 0.5 0.3
NGC4968	1.2 \pm 0.7 0.7
NGC5033	...	2.4 \pm 1.4 1.3	2.0 \pm 2.0	...	2.0 \pm 1.2 1.3	0.9 \pm 1.0 0.8
NGC5252	0.6 \pm 0.5 0.6	2.0 \pm 2.3	...
NGC526A	0.3 \pm 0.8 0.3	...
NGC5273	...	0.8 \pm 0.9 0.6	2.2 \pm 1.6 1.1	0.6 \pm 0.8 0.3
NGC5506	2.0 \pm 1.3 1.3	0.7 \pm 0.6 0.3	0.9 \pm 1.0 0.7	0.3 \pm 0.2	1.6 \pm 0.7 0.3	0.4 \pm 0.3 0.3
NGC5643	2.9 \pm 5.1 2.8	2.6 \pm 1.3 1.3	...
NGC591	0.6 \pm 0.4	...
NGC6552
NGC7172	0.3 \pm 0.4 0.2	...	0.2 \pm 0.2 0.1	...
NGC7212
NGC7214	0.8 \pm 0.7 0.5	...	0.3 \pm 0.4 0.3	...
NGC7479	0.7 \pm 0.7 0.7	...
NGC7582	1.8 \pm 1.6 1.1	...	1.0 \pm 1.0 0.6	0.3 \pm 0.5 0.3	2.3 \pm 0.6 0.7	...
NGC7674
UGC1214	1.7 \pm 1.8 1.1	1.6 \pm 2.2 1.1	3.3 \pm 2.1 1.5	0.8 \pm 1.2 0.8
UGC2456	9.8 \pm 11.0 7.6	0.9 \pm 1.1 0.7	...	1.1 \pm 0.9 0.7
UGC2608
UGC4203	12.5 \pm 13.9 9.6	1.7 \pm 2.0 1.5
UGC6527
UGC8621
UM625	...	1.0 \pm 1.1 0.8

Table 7. Best-fit fluxes for the transitions discussed in this *paper*. *Dots* indicate lines not detected.

cation of the CVI lines. Moreover, the shifted measurements do not cluster in any well defined spectral region. Uncertainties on the aspect solutions can be as high as 30Å in this wavelength range, still insufficient to explain the observed differences.

A similar analysis on the centroid energies of the RRC features shows that only 3 measurements (out of 16) of the OVII RRC are inconsistent with the laboratory energy (at the 2σ level; none for the CV or OVIII RRCs). In this case,

as discussed in Sect. 3.1, the discrepancy is probably due to confusion with the nearby FeXVII triplet.

ACKNOWLEDGMENTS

This paper is based on observations obtained with XMM-Newton, an ESA science mission with instruments and contributions directly funded by ESA Member States

Source	Cv RRC		OvII RRC		OvIII RRC	
	E_c (Å, 31.622)	σ (eV)	E_c (Å, 16.771)	σ (eV)	E_c (Å, 14.228)	σ (eV)
Circinus Galaxy	16.775 ± 0.169	< 33.2	14.182 ± 0.058	< 4.1
ESO509-G66
IC2560	16.681 ± 0.102	< 10.0
IC4395
IC4995
IIZW035
IRAS01475-0740
IRAS08572+3915
IRAS09104+4109
IRAS10214+4724
IRAS13197-1627	14.216 ± 0.116	< 4.3
IRAS15480-0344	0.045	...
MCG-5-23-16
MRK3	16.747 ± 0.042	2.2 ± 1.9	14.166 ± 0.069	< 4.8
MRK6	0.051	1.2	0.052	...
MRK331
MRK348
MRK612
MRK744
MRK993
MRK1152	< 100.7
NGC1068	31.486 ± 0.034	1.6 ± 0.2	16.817 ± 0.044	8.9 ± 0.5	14.199 ± 0.035	2.7 ± 1.1
NGC1365	31.511 ± 0.159	1.6 ± 0.2	16.775 ± 0.054	2.3 ± 2.0	14.197 ± 0.044	< 1.9
NGC1386	...	0.1	16.778 ± 0.048	1.0	0.044	...
NGC1410	0.074
NGC1614
NGC2110	14.158 ± 0.053	< 3.2
NGC2273	0.039	...
NGC2623
NGC2992
NGC34
NGC3982
NGC4138	16.775 ± 0.056	< 2.2
NGC4151	31.490 ± 0.098	2.2 ± 1.1	16.730 ± 0.035	2.1 ± 0.7	14.210 ± 0.043	4.0 ± 3.8
NGC4168	0.055	0.7	0.041	0.5	0.052	2.1
NGC424
NGC4258	16.929 ± 0.051	9.5 ± 1.4	...	12.4 ± 8.2
NGC4303	17.033 ± 0.138	< 13.9	14.197 ± 0.061	7.2
NGC4395	0.136	...	14.453 ± 0.212	< 66.6
NGC4472	14.234 ± 0.207	7.0 ± 10.4
NGC4477	17.041 ± 0.126	< 7.3	0.080	4.7
NGC449	0.125
NGC4507	16.740 ± 0.049	2.3 ± 2.2	...	8.8 ± 13.5
NGC4565	0.052	1.1	...	4.0
NGC4639
NGC4725
NGC4945	16.538 ± 0.061	< 5.0	14.232 ± 0.251	< 33.2
NGC4968	0.046	...	0.244	...
NGC5033	31.626 ± 0.190	< 6.4
NGC5252	0.176
NGC526A
NGC5273
NGC5506	31.630 ± 0.091	< 1.1	16.775 ± 0.059	< 5.6
NGC5643	0.081	...	0.080	< 22.0
NGC591
NGC6552
NGC7172
NGC7212
NGC7314
NGC7479
NGC7582	16.709 ± 0.123	< 6.3
NGC7674	0.072
UGC1214	16.897 ± 0.271	3.5 ± 5.3	...	4.8 ± 3.1
UGC2456	0.263	3.3	14.236 ± 0.061	< 5.2
UGC2608	0.051	...
UGC4203
UGC6527
UGC8621
UM625

Table 8. Best-fit wavelengths and widths for the RRCs discussed in this *paper*. *Dots* indicates either lines not detected, or lines for which no constraints can be obtained (the luminosities in Tab. 9 are calculated in this case assuming the laboratory energies.)

and the USA (NASA). This research has made use of data obtained through the High Energy Astrophysics Science Archive Research Center On-line Service, provided by the NASA/Goddard Space Flight Center and of the NASA/IPAC Extragalactic Database (NED) which is operated by the Jet Propulsion Laboratory, California Institute of Technology, under contract with the National Aeronautics and Space Administration. Discussions with A.Pollock and J.Sanz allowed us to better understand the properties of high-resolution X-ray spectra of active stars. We are deeply grateful to Dr.A.Kinkhabwala, for providing us with an updated version of his photoion code, as well as for several

enlightening and encouraging suggestions and comments. Comments and encouragement by an anonymous referee, which significantly improved the quality of this paper, are warmly acknowledged.

REFERENCES

- Band D.L., Klein R.I., Castor I.J., Nash J.K., 1990, ApJ, 362, 90
 Beiersdorfer P. Behar E., Boyce K.R., et al., 2002, ApJ, 576, L169
 Bianchi S., Guainazzi M., Chiaberge M., 2006, A&A, 448, 499
 Bianchi S., Miniutti G., Fabian A.C., Iwasawa K., 2005, MNRAS, 360, 380

Source	Cv RRC 10^{-5} ph cm $^{-2}$ s $^{-1}$	Ovii RRC 10^{-5} ph cm $^{-2}$ s $^{-1}$	Oviii RRC 10^{-5} ph cm $^{-2}$ s $^{-1}$
Circinus Galaxy	...	$2.4^{+19.3}_{-2.3}$	$2.6^{+1.7}_{-1.5}$
ESO509-G66
IC2560	...	$0.3^{+0.2}_{-0.2}$...
IC4395
IC4995
IIIZW035
IRAS01475-0740
IRAS08572+3915
IRAS09104+4109
IRAS10214+4724
IRAS13197-1627	$0.6^{+0.5}_{-0.3}$
IRAS15480-0344
MCG-5-23-16
MRK3	...	$1.6^{+0.7}_{-0.4}$	$0.9^{+0.5}_{-0.3}$
MRK6
MRK331
MRK348
MRK612
MRK744
MRK993
MRK1152	$13.6^{+27.4}_{-12.0}$
NGC1068	$67.2^{+10.1}_{-7.7}$	$65.9^{+2.1}_{-3.1}$	$10.1^{+2.7}_{-1.9}$
NGC1365	$0.8^{+0.5}_{-0.5}$	$1.1^{+0.5}_{-0.3}$	$0.5^{+0.3}_{-0.2}$
NGC1386	...	$0.3^{+1.3}_{-0.3}$...
NGC1410
NGC1614
NGC2110	$1.4^{+0.6}_{-0.5}$
NGC2273
NGC2623
NGC2992
NGC34
NGC3982	$1.1^{+1.4}_{-0.8}$
NGC4138	...	$0.4^{+0.4}_{-0.3}$...
NGC4151	$13.9^{+8.5}_{-7.1}$	$5.7^{+1.2}_{-1.0}$	$4.3^{+6.4}_{-1.6}$
NGC4168
NGC424
NGC4258	...	$7.6^{+0.8}_{-2.4}$...
NGC4303	...	$1.4^{+1.5}_{-1.0}$	$0.3^{+0.3}_{-0.2}$
NGC4395	$0.4^{+1.8}_{-0.3}$
NGC4472	$22.3^{+0.3}_{-16.0}$
NGC4477	...	$1.6^{+1.8}_{-1.0}$...
NGC449
NGC4507	...	$1.7^{+0.6}_{-0.6}$...
NGC4565
NGC4639
NGC4725	...	$0.3^{+0.3}_{-0.2}$...
NGC4945
NGC4968
NGC5033	$1.4^{+2.5}_{-1.2}$
NGC5252
NGC526A
NGC5273
NGC5506	$1.4^{+1.0}_{-1.1}$	$0.9^{+0.4}_{-0.5}$...
NGC5643	...	$2.0^{+0.5}_{-1.7}$...
NGC591
NGC6552
NGC7172
NGC7212
NGC7314
NGC7479
NGC7582	...	$0.5^{+0.4}_{-0.3}$	$0.7^{+0.6}_{-0.4}$
NGC7674
UGC1214	...	$1.5^{+1.5}_{-0.9}$...
UGC2456	$1.2^{+1.1}_{-0.8}$
UGC2608
UGC4203
UGC6527
UGC8621
UM625

Table 9. Best-fit fluxes for the RRCs discussed in this *paper*. *Dots* indicate lines not detected.

- Blustin A.J., et al., 2003, A&A, 403, 481
 Blustin A.J., Page M.J., Fürst S.V., et al., 2005, A&A, 431, 111
 Brinkman A.C., Kaastra J.C., van der Meer R.J.L., Kinkhabwala A., Behar E., Kahn S., Paerels F.B.S., Sako M., 2002, A&A, 396, 761
 Brown G.V., Beiersdorfer P., Liedhal D.A., Widmann K., 1998, ApJ, 502, 1015
 Cid Fernandes R., Storchi-Bergman T., Schmitt H.R., 1998, ApJ, 501, 94
 Cid Fernandes R., Heckman T., Schmitt H., González-Delgado R.M., Storchi-Bergmann T., 2001, 558, 81
 Dere K.P., Landi E., Del Zanna G., Young P.R., 2001, ApJSS, 134, 331
 der Herder J., et al., 2001, A&A, 365, L7
 Dickey J.M., Lockman F.J., 1990, ARA&A 28, 215
 Gabriel A.H., Jordan C., 1969, MNRAS, 145, 241
 Gabriel C., Denby M., Fyfe D. J., Hoar J., Ibarra A., 2003, in ASP Conf. Ser., Vol. 314 ADASS XIII, eds. F. Ochsenbein, M. Allen, & D. Egret (San Francisco: ASP), 759
 Gonzalez Delgado R., Heckman T., Leitherer C., 2001, ApJ, 546, 845
 Guainazzi M., Matt G., Perola G.C., 2005, A&A, 444, 119
 Kallman T.R., Liedahl D., Osterheld A., Goldstein W., Kahn S., 1996, ApJ, 465, 994
 King A.R., 2005, ApJ, 635, L121
 Kinkhabwala A., et al., 2002, ApJ, 575, 732
 Krolik J.H., Kriss G.A., 1995, ApJ, 447, 512
 Levenson N.A., Krolik J.H., Zycki P.T., Heckman T.M., Weaver

- K.A., Awaki H., Terashima Y., 2002, ApJ, 573, L81
Liedahl D.A., Paerels F., 1996, ApJ, 469, L33
Matt G., 1994, MNRAS, 267, L17
Mauche C.W., Liedahl D.A., Fournier K.B., 2001, ApJ, 560, 992
Phillips K.J.H., Greer C.J., Bhatia A.K., Coffey I.H., Barnsley R., Keenan F.P., 1997, A&A, 324, 381
Porquet D., Dubau J., 2000, A&AS, 143, 495
Pounds K.A., Page K.L., 2005, MNRAS, 360, 1123
Sambruna R., Netzer H., Kaspi S., Brandt W.N., Chartas G., Garmire G.P., Nousek J.A., Weaver K.A., 2001, ApJ, 546, L13
Sako M., Kahn S.M., Paerels F., Liedahl D.A., 2000, ApJL 543, L115
Schmitt J.H.M.M., 1985, A&A, 293, 178
Schurch N.J., Warwick R.S., Griffiths R.E, Kahn S.M., 2004, MNRAS, 350, 1
Steenbrugge K.C., et al., 2005, A&A, 434, 569
Turner T.J., George I.M., Nandra K., Mushotzky R.F., 1997, ApJS 113, 23
Young A.J., Wilson A.S., Shopbell P.L., 2001, ApJ, 556, 6
Wu W., Clayton G.C., Gordon K.D., Misselt K.A., Smith T.L., Calzetti D., 2002, ApJS, 143, 377